

# Non-Invasive Reconstruction of Intracranial EEG Across the Deep Temporal Lobe from Scalp EEG based on Conditional Normalizing Flow

Dongyi He<sup>a</sup>, Bin Jiang<sup>a,\*</sup>, Kecheng Feng<sup>a</sup>, Luyin Zhang<sup>a</sup>, Ling Liu<sup>a</sup>, Yuxuan Li<sup>a</sup>, Yun Zhao<sup>b</sup>, He Yan<sup>a</sup>

<sup>a</sup>*School of Artificial Intelligence, Chongqing University of Technology, Chongqing, 400054, China*

<sup>b</sup>*School of Smart Health, Chongqing Polytechnic University of Electronic Technology, Chongqing, 401331, China*

---

## Abstract

Although obtaining deep brain activity from non-invasive scalp electroencephalography (sEEG) is crucial for neuroscience and clinical diagnosis, directly generating high-fidelity intracranial electroencephalography (iEEG) signals remains a largely unexplored field, limiting our understanding of deep brain dynamics. Current research primarily focuses on traditional signal processing or source localization methods, which struggle to capture the complex waveforms and random characteristics of iEEG. To address this critical challenge, this paper introduces NeuroFlowNet, a novel cross-modal generative framework whose core contribution lies in the first-ever reconstruction of iEEG signals from the entire deep temporal lobe region using sEEG signals. NeuroFlowNet is built on Conditional Normalizing Flow (CNF), which directly models complex conditional probability distributions through reversible transformations, thereby explicitly capturing the randomness of brain signals and fundamentally avoiding the pattern collapse issues common in existing generative models. Additionally, the model integrates a multi-scale architecture and self-attention mechanisms to robustly capture fine-grained temporal details and long-range dependencies. Validation results on a publicly available synchronized sEEG-iEEG dataset demonstrate NeuroFlowNet's effectiveness in terms of temporal waveform fidelity, spectral feature reproduction, and functional connectivity restoration. This study establishes a more reliable and scalable new paradigm for non-invasive analysis of deep brain dynamics. The code of this study is available in <https://github.com/hdy6438/NeuroFlowNet>

**Keywords:** Deep brain activity, Intracranial electroencephalography (iEEG), Scalp electroencephalography (sEEG), Cross-modal generation, Generative models, Brain signal reconstruction,

---

## 1. Introduction

Electroencephalography (EEG) is a high-time-resolution brain activity monitoring technique that can track neuronal activation in real time and dynamically record brain activity. It plays a crucial role in brain-computer interfaces, clinical diagnosis, and cognitive neuroscience research [1, 2]. Among these, scalp electroencephalography (sEEG) measures the distribution of potentials on the scalp resulting from the propagation of postsynaptic potentials and action potentials from neuronal clusters in the brain, as detected by electrodes placed on the scalp [3]. It offers the advantages of simplicity and high flexibility, making it widely used in clinical monitoring and diagnosis [4]. However, due to the influence of cranial volume conduction effects during signal propagation, its spatial resolution is relatively low [5, 6]. That is, the measured signals represent the superimposed potentials formed by the activities of numerous sources within the brain on the scalp surface. These signals are characterized by weak potentials, susceptibility to external noise interference, and low signal-to-noise ratios, making it difficult to accurately decode the complex dynamic relationships of deep brain neural activities [7, 8]. This limitation restricts its further application in clinical settings. In contrast, intracranial electroencephalography (iEEG) can directly obtain neural activity signals from the cerebral cortex or deep nuclei, featuring high temporal-spatial resolution and high signal-to-noise ratio [9]. It is the gold standard for locating lesions in brain-related diseases and achieving high-precision neural decoding [10, 11]. However,

---

\*Corresponding author. Email: [jb20200132@cqut.edu.cn](mailto:jb20200132@cqut.edu.cn)

its high surgical costs and the risks of immune reactions and infections following electrode implantation significantly limit its practical application [10].

Given the limited spatial resolution of sEEG and the difficulty in obtaining iEEG signals, the brain electroencephalogram inverse problem has emerged as a research hotspot to achieve real-time monitoring and precise localization of neuronal activity [12, 13, 14]. Its core lies in how to infer the spatial distribution and temporal information of cortical and deep neuronal electrical activity from sEEG signals recorded on the scalp [12, 3]. By solving the EEG inverse problem, it is possible to map non-invasive sEEG signals to neural signals of approximately iEEG quality [15, 16]. This not only helps to “unlock” dynamic information from deep brain regions under non-invasive conditions [17] but also provides new technical support for precise localization of epileptic foci, analysis of brain functional mechanisms, and neural rehabilitation interventions [18].

However, significant differences in discharge patterns and signal characteristics between sEEG and iEEG limit the effectiveness of traditional methods [19, 20]. Parameter-based localization methods based on equivalent current dipoles (ECD) are constrained by the difficulty in accurately estimating the number of dipoles [3, 21], while source reconstruction methods based on current distribution are hindered by discrepancies between prior constraints and actual neuronal activity [22], both of which struggle to accurately reconstruct complex neural dynamics [23, 24]. Additionally, traditional machine learning methods rely on manual feature extraction [25, 26] and have limited nonlinear modeling capabilities [25], further restricting their representation capabilities in EEG inversion.

In recent years, deep learning techniques have significantly improved EEG inversion performance through their powerful nonlinear fitting capabilities [27, 28, 29]. For example, convolutional neural networks (CNNs) extract spatial correlations between multiple channels through spatial convolution, enhancing the accuracy of source space imaging [30, 31, 32]. Recurrent neural networks (RNNs) and their variants can model the temporal dynamic characteristics of signals, significantly improving the ability to distinguish between transient and sustained source activity [33, 34]. However, deep learning methods still face numerous challenges. Due to data limitations, model training often relies on large-scale synthetic data generated using finite element or boundary element models [35]. Synthetic data struggles to fully reflect the true complex mapping relationship between sEEG and deep neuronal electrical activity, severely limiting the model’s performance in real clinical applications. Additionally, the outputs of this method are primarily continuous neural activity distribution maps, which can locate positions but struggle to capture neural response waveforms, thereby impacting further decoding analysis [36].

Generative models offer a new approach for high-fidelity mapping from sEEG signals to iEEG signals, with the core mechanism being the use of generative networks to perform cross-modal conversion of easily obtainable non-invasive sEEG signals into iEEG signals. Abdi-Sargezeh et al. were the first to introduce generative adversarial networks (GANs) to address this issue [37], successfully generating high-quality iEEG waveforms while demonstrating advantages in terms of efficiency and model complexity. Building on this, they proposed an EEG-to-EEG conversion model, named VAE-cGAN [38], combining variational autoencoders (VAE) and conditional generative adversarial networks (cGAN), and validated it on a dataset containing real iEEG signals recorded via Foramen Ovale electrodes. By encoding sEEG into the latent space and regenerating iEEG signals, they further enhanced the fidelity and signal resolution of the mapped waveforms. The team achieved waveform reconstruction for the first time under conditions where real iEEG was used as a reference, providing a new technical pathway for non-invasive acquisition of high-fidelity iEEG signals. However, this research remains in its preliminary exploratory phase. Due to limitations such as the sampling range of Foramen Ovale channels and inherent defects like mode collapse in GAN models, current reconstruction is only feasible for localized regions of the medial temporal lobe (MTL), and expanding the number of reconstruction channels may significantly degrade reconstruction quality and effectiveness. Additionally, expanding the number of reconstructed channels may significantly degrade reconstruction quality and effectiveness. Additionally, due to the complexity and randomness of neural activity in the brain, models like GAN and VAE, which use deterministic mappings, often fail to adequately reflect the spatiotemporal diversity and randomness of iEEG signals.

To address these challenges, this study innovatively proposes a new cross-modal generative framework named NeuroFlowNet, which attempts for the first time to reconstruct iEEG signals across the entire deep temporal lobe region using sEEG. To capture the spatio-temporal diversity and randomness of iEEG signals, the model is based on Conditional Normalizing Flow (CNF), directly learning the complex conditional probability distribution  $p(X_{iEEG}|X_{sEEG})$  from sEEG to iEEG. Compared to traditional deterministic mappings, the normalizing flow model precisely maps complex data distributions to simple prior distributions (such as Gaussian distributions) through a series of reversible

# NeuroFlowNet

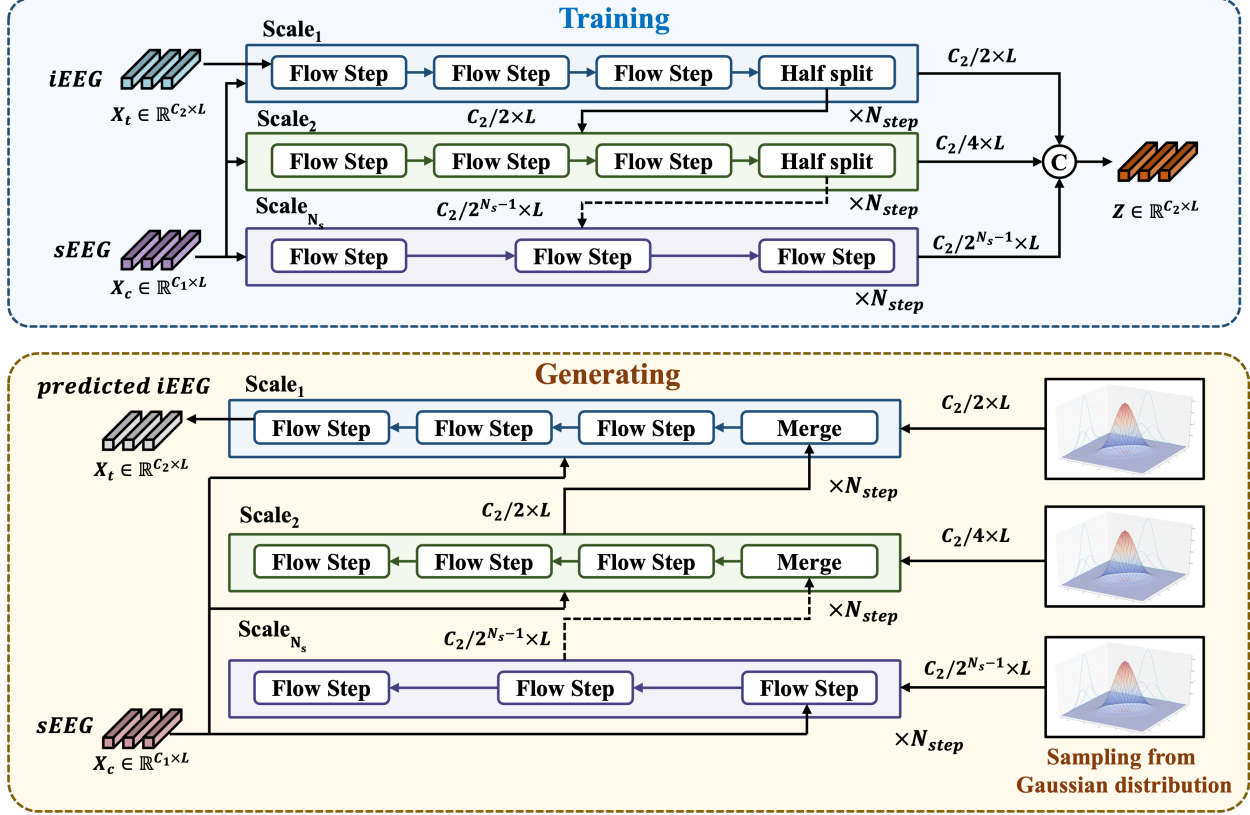


Figure 1: Overview of NeuroFlowNet architecture. The model consists of multiple scales, each containing a series of flow steps that transform the iEEG data conditioned on the sEEG data. The final latent variable  $Z$  is obtained by concatenating the outputs from all scales.

transformations, enabling the generation of more diverse and probabilistically realistic iEEG samples. This effectively addresses the issue of existing methods ignoring the inherent randomness of brain activity and avoids the pattern collapse phenomenon that may occur during model training. Additionally, the model adopts a multi-scale architecture combined with self-attention mechanisms, further enhancing the fineness and robustness of iEEG waveform reconstruction. NeuroFlowNet has been validated for effectiveness on a publicly available dataset [39] of whole temporal lobe sEEG-iEEG signals synchronously collected via Stereoelectroencephalography electrodes. Experimental results demonstrate that the model has advantages in signal fidelity, spectral feature reproduction, and network structure recovery. This provides a more precise and reliable new paradigm for non-invasive analysis of deep brain dynamics.

## 2. Methods

The proposed model, NeuroFlowNet, demonstrated in Figure 1, is designed to generate iEEG signals from non-invasive sEEG signals by learning the conditional probability distribution of iEEG given EEG,  $p(X_t|X_c)$ , where  $X_t \in \mathbb{R}^{C_{out} \times L}$  represents the target iEEG signals and  $X_c \in \mathbb{R}^{C_{in} \times L}$  represents the conditioning sEEG signals, with  $C_{out}$  and  $C_{in}$  being the number of channels of iEEG and sEEG, respectively, and  $L$  denoting the temporal length of the signals. NeuroFlowNet is architected as a multi-scale conditional normalizing flow, which transforms the complex distribution of iEEG data, conditioned on sEEG data, into a simple, tractable base distribution (typically a standard multivariate Gaussian) via a sequence of invertible and differentiable transformations. The conditioning on sEEG signals  $X_c$  is achieved through a series of coupling layers, where the transformation is conditioned on the sEEG data. The model

is trained using a maximum likelihood estimation approach, optimizing the parameters of the transformations to maximize the likelihood of the observed iEEG data given the sEEG data.

### 2.1. Core Invertible Transformation: Conditional Affine Coupling Layer

The core of the NeuroFlowNet architecture is the conditional affine coupling layer, which allows for the transformation of the iEEG data while conditioning on the sEEG data. The coupling layer operates by splitting the input data into two parts: one part is transformed while the other part through an identity transformation. Specifically, given an input vector  $x \in \mathbb{R}^{C \times L}$  at any stage of the flow, it is first split along the channel dimension into two halves,  $x_a \in \mathbb{R}^{C/2 \times L}$  and  $x_b \in \mathbb{R}^{C/2 \times L}$ . The first half,  $x_a$ , is passed through an identity transformation, while the second half,  $x_b$ , is transformed using a conditional affine transformation parameterized by a neural network. The transformation can be expressed as:

$$z_b = (x_b + \tau) \odot \exp(\sigma) \quad (1)$$

where  $\odot$  denotes element-wise multiplication. The translation parameters  $\tau \in \mathbb{R}^{C/2 \times L}$  and the log-scale parameters  $\sigma \in \mathbb{R}^{C/2 \times L}$  are produced by a conditional neural network, denoted as  $g_{cond}$ , which takes  $x_a$  and the conditioning sEEG data  $X_c$  as inputs, and outputs the parameters  $\tau$  and  $\sigma$ :

$$\begin{bmatrix} \tau \\ \sigma \end{bmatrix} = g_{cond}(x_a, X_c) \quad (2)$$

The conditional neural network  $g_{cond}$  is designed to capture the complex relationships between the iEEG and sEEG data, allowing for a more accurate transformation of the iEEG data based on the conditioning sEEG data. The  $g_{cond}$  network is composed of an initial couple of convolutional layers with kernel size of 3 and 1, respectively, both followed by a ReLU activation function. The output of the convolutional layers is then passed through a multi-head self-attention mechanism, which allows the model to capture long-range dependencies in the data, complementary to the local features captured by the convolutional layers. The self-attention mechanism is implemented using the scaled dot-product attention, which computes the attention scores based on the dot product of the query and key vectors, followed by a softmax operation to obtain the attention weights. The attention weights are then used to compute a weighted sum of the value vectors, producing the final output of the self-attention mechanism, expressed as:

$$\text{Attention}(Q, K, V) = \text{softmax}\left(\frac{QK^T}{\sqrt{d_k}}\right)V \quad (3)$$

where  $Q$ ,  $K$ , and  $V$  are the query, key, and value matrices, respectively, and  $d_k$  is the dimensionality of the key vectors.

The multi-head self-attention mechanism allows the model to capture multiple relationships between the input data and the conditioning data by using multiple sets of query, key, and value matrices, each with different learned parameters. The output of the attention mechanism is then passed through a final convolutional layer with kernel size of 3 to produce the final parameters  $\tau$  and  $\sigma$ . For numerical stability, translation parameters  $\tau$  is scaled by a hyperbolic tangent function ( $\tanh$ ) to ensure that the values are bounded between -1 and 1, while the log-scale parameters  $\sigma$  are clipped to a range of [-5, 5] to prevent numerical instability during the training process. The log-determinant of the Jacobian for this affine transformation is given by the sum of the log-scale factors:

$$\log \left| \det \frac{\partial z_b}{\partial x_b} \right| = \sum_{i,j} \sigma_{i,j} \quad (4)$$

The output of the coupling layer is  $z = \text{concatenate}(x_a, z_b)$ . The inverse transformation is obtained by applying the inverse of the affine transformation, which can be expressed as:

$$x_b = \exp(-\sigma) \odot (z_b - \tau) \quad (5)$$

where the inverse transformation is applied to the transformed data  $z_b$  to recover the original data  $x_b$ .

The inverse transformation is also computed in a similar manner, where the translation and log-scale parameters are obtained from the same conditional neural network  $g_{cond}$ , but with the input data being the transformed data  $z_a$  and the conditioning sEEG data  $X_c$ , i.e.:

$$\begin{bmatrix} \tau \\ \sigma \end{bmatrix} = g_{cond}(z_a, X_c) \quad (6)$$

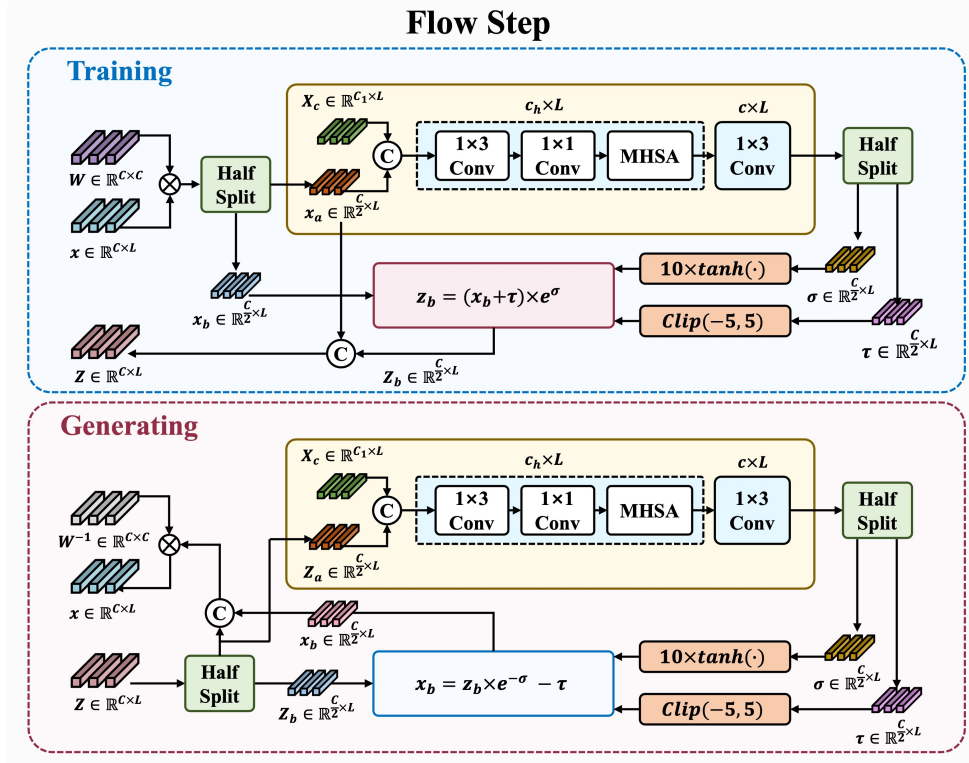


Figure 2: Flow step composition in NeuroFlowNet. Each flow step consists of an invertible  $1 \times 1$  convolution followed by a conditional affine coupling layer, which transforms the input data while conditioning on the sEEG data.

## 2.2. Flow Step Composition

As demonstrated in Figure 2, each flow step within NeuroFlowNet combines the conditional affine coupling layer with an invertible channel-mixing operation to enhance the expressive power of the model. Specifically, before the input  $x$  is fed into the affine coupling layer, it undergoes an invertible  $1 \times 1$  convolutional operation, a channel-wise linear transformation,  $y = Wx'$ , where  $x'$  is the input to the flow step and  $W \in \mathbb{R}^{C \times C}$  is a learnable weight matrix, which is initialized as an orthonormal matrix (via QR decomposition of a random Gaussian matrix) to ensure invertibility from the start of training and promote stability. This  $1 \times 1$  convolution allows for information to be mixed across channels at each temporal location independently. The log-determinant of the Jacobian for this transformation is:

$$\log \left| \det \frac{\partial y}{\partial x'} \right| = L \cdot \log |\det W| \quad (7)$$

The total log-determinant for a single flow step is the sum of the log-determinants from the  $1 \times 1$  convolution and the subsequent conditional affine coupling layer. The inverse of the flow step involves applying the inverse affine coupling transformation followed by multiplication with  $W^{-1}$ .

## 2.3. Multi-Scale Architecture

The proposed NeuroFlowNet employs a multi-scale architecture to effectively model features and dependencies at varying resolutions within the iEEG signals. The model comprises  $N_S$  hierarchical scales. At each scale  $k \in \{1, \dots, N_S\}$ , the input, target iEEG signal  $X_t$  at the first scale or the output from the preceding finer scale ( $k - 1$ ), is processed through a sequence of  $N_{\text{steps}}$  identical flow steps, as detailed in Section 2.2, with all transformations are conditioned on the sEEG signal  $X_c$ .

Following the flow steps at scale  $k$ , the resulting tensor  $y^{(k)} \in \mathbb{R}^{C_k \times L}$  is split along the channel dimension. A subset of channels,  $z_{\text{part}}^{(k)} \in \mathbb{R}^{C_k/2 \times L}$ , is extracted and designated as part of the final latent variable  $Z$ . The remaining channels,

$x_{in}^{(k+1)} \in \mathbb{R}^{C_k/2 \times L}$ , are propagated as input to the subsequent, typically coarser, scale  $(k + 1)$ . The number of channels  $C_k$  is halved at each successive scale, facilitating a progressive abstraction of features.

This hierarchical processing strategy enables the model to decompose the learning task, capturing fine-grained details at the initial scales and progressively more abstract, global representations at deeper levels. The final output from the coarsest scale,  $z_{final}^{(N_S)} \in \mathbb{R}^{C_{N_S} \times L}$ , also contributes to the complete latent representation. The full latent variable  $Z$  is obtained by concatenating all extracted components and the final output:

$$Z = \text{concatenate}(z_{part}^{(1)}, z_{part}^{(2)}, \dots, z_{part}^{(N_S-1)}, z_{final}^{(N_S)}) \in \mathbb{R}^{C_{out} \times L} \quad (8)$$

where  $C_{out} = \sum_{k=1}^{N_S} C_k/2 + C_{N_S}$  is the total number of channels in the latent variable  $Z$

## 2.4. Training and Inference

### 2.4.1. Training

NeuroFlowNet is trained by maximizing the exact log-likelihood of the iEEG data  $X_t$  given the sEEG context  $X_c$ . Algorithm 1 outlines the training procedure. Let  $f$  denote the overall transformation from the data space to the latent space, such that  $Z = f(X_t, X_c)$ . The log-likelihood of the iEEG data can be expressed as:

$$\log p(X_t | X_c) = \log p_Z(Z) + \sum_{i=1}^M \log \left| \det \frac{\partial z_i}{\partial z_{i-1}} \right| \quad (9)$$

where  $M$  is the total number of elementary invertible transformations that map the input  $X_t$  to the final latent variable  $Z$  (as defined in Equation 8),  $z_0 = X_t$  and  $z_i$  is the output of the  $i$ -th transformation acting on its input  $z_{i-1}$ , then the final result of these  $M$  transformations is  $Z$ . The term  $\frac{\partial z_i}{\partial z_{i-1}}$  is the Jacobian matrix of this  $i$ -th transformation.  $p_Z(Z)$  is the log-probability density of  $Z$  under a standard multivariate Gaussian distribution  $\mathcal{N}(0, I)$ , which serves as the base distribution. The sum term  $\sum_{i=1}^M \log \left| \det \frac{\partial z_i}{\partial z_{i-1}} \right|$  is the accumulated sum of the log-determinants of these Jacobians for all constituent invertible transformations ( $1 \times 1$  convolutions and affine coupling layers) across all flow steps and scales.

The model parameters are optimized by maximizing this log-likelihood objective:

$$\theta^* = \arg \max_{\theta} \log p(X_t | X_c; \theta) \quad (10)$$

where  $\theta$  represents the parameters of the model, including the weights of the conditional neural network  $g_{cond}$  and the weights of the  $1 \times 1$  convolutions.

### 2.4.2. Inference (iEEG Generation)

To generate iEEG samples  $\hat{X}_t$  conditioned on a given sEEG signal  $X_c$ , the inverse transformation  $f^{-1}$  is employed. Algorithm 2 outlines the inference procedure. First, a sample  $\hat{Z}$  is drawn from the base Gaussian distribution  $p_Z(Z)$ . This  $\hat{Z}$  is then partitioned into segments  $\hat{z}_{part}^{(1)}, \dots, \hat{z}_{part}^{(N_S-1)}, \hat{z}_{final}^{(N_S)}$  corresponding to the multi-scale splitting performed during the forward pass. The generation process starts from the coarsest scale  $N_S$ . The segment  $\hat{z}_{final}^{(N_S)}$  is transformed by applying the inverse of the flow steps within the  $N_S$ -th scale block. For each subsequent finer scale  $k$  (iterating from  $N_S - 1$  down to 1), the corresponding latent segment  $\hat{z}_{part}^{(k)}$  is concatenated with the output from the inverse transformation of the preceding coarser scale  $(k + 1)$ . This combined tensor is then passed through the inverse flow steps of scale  $k$ . All inverse transformations are conditioned on the sEEG context  $X_c$ . The final output of this sequential inverse process, after passing through the inverse of the first scale block, is the generated iEEG sample  $\hat{X}_t = f^{-1}(\hat{Z}; X_c)$ .

## 3. Experiments

### 3.1. Dataset

This study utilizes an electrophysiological dataset recorded from nine epilepsy patients during a verbal working memory task, as introduced by Boran et al. [39], which is publicly available at [https://gin.g-node.org/USZ\\_NCH/Human\\_MTL\\_units\\_scalp\\_EEG\\_and\\_iEEG\\_verbal\\_WM](https://gin.g-node.org/USZ_NCH/Human_MTL_units_scalp_EEG_and_iEEG_verbal_WM). The dataset includes simultaneous sEEG recorded using the 10-20 system and iEEG obtained via depth microelectrodes implanted in the medial temporal lobe (MTL).

---

**Algorithm 1** Training Phase of NeuroFlowNet (Forward & Parameter Update)

---

**Require:** Batch  $\{X_c, X_t\}$ , model parameters  $\theta$ , per-scale splits  $\{S_k\}_{k=1}^K$ , time length  $L$

**Ensure:** Updated parameters  $\theta$  by maximizing  $\log p(X_t | X_c)$

```
1: Initialize  $\log\_det\_total \leftarrow \mathbf{0}_B$ ,  $o \leftarrow X_t$ ,  $\mathcal{Z} \leftarrow \emptyset$ 
2: for  $k = 1 \rightarrow K$  do
3:    $\log\_det_k \leftarrow \mathbf{0}_B$ 
4:   for  $i = 1 \rightarrow N_k$  do ▷ FlowStep  $i$  in scale  $k$ 
5:      $u \leftarrow 1 \times 1 \text{conv}_{W_i^{(k)}}(o)$ 
6:      $\Delta_{\text{conv}} \leftarrow L \cdot \text{slogdet}(W_i^{(k)})$  ▷ scalar
7:      $[u_a, u_b] \leftarrow \text{split\_half}(u)$ 
8:      $[\tau, \sigma] \leftarrow g_{\text{cond}}(u_a, X_c; \theta_{\text{aff}})$ 
9:      $\tau \leftarrow 10 \cdot \tanh(\tau)$ ,  $\sigma \leftarrow \text{clamp}(\sigma, -5, 5)$ 
10:     $z_b \leftarrow (u_b + \tau) \odot \exp(\sigma)$ 
11:     $o \leftarrow \text{concat}(u_a, z_b)$ 
12:     $\Delta_{\text{affine}} \leftarrow \sum_{c,t} \sigma_{c,t}$  ▷ per-sample vector of size  $B$ 
13:     $\log\_det_k \leftarrow \log\_det_k + (\Delta_{\text{conv}} + \Delta_{\text{affine}})$ 
14:  end for
15:   $z^{(k)} \leftarrow o[:, 1 : S_k, :]$  ▷ extract latent part
16:   $o \leftarrow o[:, S_k + 1 : C_k, :]$  ▷ remaining channels to next scale
17:  append  $z^{(k)}$  to  $\mathcal{Z}$ 
18:   $\log\_det\_total \leftarrow \log\_det\_total + \log\_det_k$ 
19: end for
20: append final  $o$  to  $\mathcal{Z}$  ▷ final leftover latent
21:  $Z \leftarrow \text{concat}(\mathcal{Z}, \text{channel})$ 
22:  $\log p_Z \leftarrow -\frac{1}{2} \sum_{c,t} (Z^2 + \log(2\pi))$  ▷ per-sample
23:  $\mathcal{L} \leftarrow -\frac{1}{B} \sum_{b=1}^B (\log p_Z^{(b)} + \log\_det\_total^{(b)})$ 
24: Backpropagate  $\mathcal{L}$  and update  $\theta$  (e.g., AdamW step)
```

---

The sEEG and iEEG signals are originally sampled at 256 Hz and 4 kHz, respectively, and later resampled to 200 Hz and 2 kHz. It also contains waveforms and spike times of 1526 single units, along with MNI coordinates in MNI152 space and anatomical labels for the intracranial electrodes.

The nine subjects (five female, four male) are all right-handed and aged between 18 and 56. Their pathologies include hippocampal sclerosis, gliosis, xanthoastrocytoma, brain contusion, and focal cortical dysplasia. Each participant has a varying number and location of implanted depth electrodes within the MTL. Due to significant inter-subject variability in electrode implantation (both in terms of anatomical coverage and number of recorded units), only subjects S1, S6, and S9 were included in this study. These three subjects were selected because (i) they have comprehensive electrode coverage across key MTL subregions of interest, (ii) they exhibit a sufficient number of well-isolated single units for reliable statistical analysis, and (iii) their recording sessions contained minimal artifacts and consistent task performance. Due to clinical considerations and individualized implantation plans, the exact anatomical locations of intracranial electrodes differ across subjects [39]. To illustrate this variability, Figure 3 presents a 3D schematic of depth electrode trajectories in the MTL for three subjects (S1, S6 and S9) used in this study.

Each subject completes between two and seven recording sessions. Table 1 summarizes the characteristics of the subjects, including their personal information, pathologies, implanted scalp and intracranial electrodes, and number of sessions. The sEEG signals are recorded using the international 10-20 system, with electrodes placed at standard locations such as Fp1, Fp2, F7, F3, Cz, Pz, O1, and O2. The iEEG signals are recorded from depth microelectrodes targeting multiple MTL subregions: anterior hippocampus (AHL/AHR), amygdala (AL/AR), entorhinal cortex (ECL/ECR), and parahippocampal gyrus (PHL/PHR), as well as lateral rhinal area (LR). Each trajectory consisted of eight microelectrode contacts arranged along a single stereotactic path.

The dataset provides a rich source of electrophysiological data, allowing for the exploration of cross-modal generation of iEEG signals from sEEG signals. The iEEG signals are used as the target signals  $X_t$  for model training

---

**Algorithm 2** Inference / Sampling Phase of NeuroFlowNet (Inverse Mapping)

---

**Require:** Conditioning  $X_c$ , model parameters  $\theta$ , per-scale splits  $\{S_k\}_{k=1}^K$ , optional  $\varepsilon \in \mathbb{R}^{B \times D \times L}$

**Ensure:** Generated iEEG samples  $\hat{X}_t$

```
1: if no  $\varepsilon$  provided then
2:   sample  $\varepsilon \sim \mathcal{N}(0, I)$  ▷ shape matches total latent channels
3: end if
4: split  $\varepsilon$  into parts  $\{\tilde{z}^{(1)}, \dots, \tilde{z}^{(K)}, \tilde{z}^{(K+1)}\}$  according to  $\{S_k, \dots\}$ 
5:  $o \leftarrow \tilde{z}^{(K+1)}$  ▷ start from coarsest latent
6: for  $k = K \rightarrow 1$  do ▷ reverse through scales
7:    $o \leftarrow \text{concat}(\tilde{z}^{(k)}, o)$  ▷ reconstruct full channel tensor at scale  $k$ 
8:   for each FlowStep  $i = N_k, \dots, 1$  (reversed order) do
9:      $[z_a, z_b] \leftarrow \text{split\_half}(o)$ 
10:     $[\tau, \sigma] \leftarrow g_{\text{cond}}(z_a, X_c; \theta_{\text{aff}})$ 
11:     $\tau \leftarrow 10 \cdot \tanh(\tau)$ ,  $\sigma \leftarrow \text{clamp}(\sigma, -5, 5)$ 
12:     $u_b \leftarrow \exp(-\sigma) \odot (z_b - \tau)$  ▷ affine inverse
13:     $u \leftarrow \text{concat}(z_a, u_b)$ 
14:     $o \leftarrow 1 \times 1 \text{conv}_{W^{-1}}(u)$  ▷ apply inverse 1x1 conv
15:   end for
16: end for
17: Output:  $\hat{X}_t \leftarrow o$ 
```

---

and evaluation, while the sEEG signals are used as the conditioning input  $X_c$ . The dataset is suitable for training and evaluating the NeuroFlowNet model, as it contains a diverse set of subjects with varying pathologies and electrode placements. The model aims to learn the complex relationships between the non-invasive sEEG signals and the invasive iEEG signals, enabling the generation of iEEG signals from sEEG data.

### 3.2. Data Preprocessing and Division

The iEEG and sEEG signals are preprocessed to remove artifacts and noise, ensuring high-quality data for model training. The preprocessing steps include wavelet denoising, downsampling, data division, and normalization.

The wavelet denoising is performed using the discrete wavelet transform (DWT) with Symmetric Wavelet (Symlet) wavelets of order 4, which are effective in preserving the signal’s features while removing noise. The three-level DWT decomposes the signal into approximation and detail coefficients, allowing for selective thresholding of the detail coefficients to remove noise. Specifically, the approximation coefficients are retained, while the detail coefficients are thresholded using a soft thresholding method. The threshold is determined based on the noise level in the signal, which is estimated using the median absolute deviation (MAD) of the detail coefficients. The denoised signal is then reconstructed by applying the inverse discrete wavelet transform (IDWT) to the modified coefficients. The downsampling operation is performed to reduce the sampling rate of the iEEG signals from 2 kHz to 200 Hz, matching the sampling rate of the sEEG signals.

Each subject participates in multiple recording sessions, with each session consisting of multiple trials of a verbal working memory task. Within each session, randomly select 90% of the trials for training and the remaining 10% for validation. The training and validation sets are further divided into smaller segments of 200 samples (1 second) used a sliding window approach with a 90% overlap for training sets, while the validation set is divided into segments of 200 samples with no overlap. The Z-score normalization is applied to each segment, ensuring that the mean and standard deviation of the signals are zero and one, respectively. This normalization step is crucial for stabilizing the training process and improving the model’s performance.

### 3.3. Implementation Details

The NeuroFlowNet model is implemented using PyTorch, a popular deep learning framework. The model architecture consists of multiple scales, each containing a series of flow steps that transform the iEEG data conditioned on the sEEG data. The model is trained using the AdamW optimizer with a learning rate of  $1 \times 10^{-3}$  and a weight decay

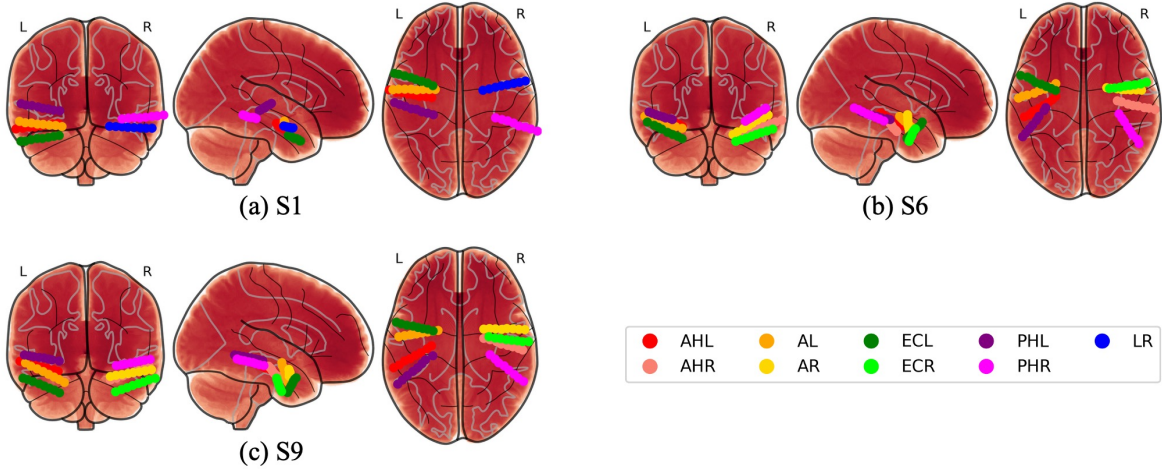


Figure 3: Medial temporal lobe (MTL) depth electrode locations for subjects used in this study (S1, S6 and S9). Each panel shows coronal, sagittal, and axial views of depth electrode trajectories within MTL subregions. Colors indicate anatomical targets: anterior hippocampus (AHL/AHR, red/light red), amygdala (AL/AR, orange/yellow), entorhinal cortex (ECL/ECR, green/light green), parahippocampal gyrus (PHL/PHR, purple/magenta), and lateral rhinal area (LR, blue). Each trajectory consists of eight electrode contacts positioned along a single stereotactic path.

of  $1 \times 10^{-2}$ . The model is trained on a single NVIDIA RTX 4080 GPU with 16 GB of memory. The batch size is set to 128, and the model is trained for 100 epochs. Early stopping is implemented based on the performance on the validation set, with a patience of 10 epochs.

## 4. Results and Discussion

The performance of NeuroFlowNet is evaluated based on its ability to generate iEEG signals from sEEG signals in terms of temporal waveform, power spectral density (PSD) waveform, alpha PSD waveform and functional connection mode. The results reveal a clear pattern of region- and subject-specific variability, reflecting both the strengths and current limitations of the model.

### 4.1. Temporal Waveform Comparison

A qualitative assessment of the model’s performance is presented in Figure 4, which displays exemplar generated iEEG signals (orange) overlaid with the corresponding ground truth iEEG signals (blue) for a 200ms segment from Subject S6. The figure provides a visual comparison across various MTL subregions, including the anterior hippocampus (AHL/AHR), amygdala (AL/AR), entorhinal cortex (ECL/ECR), and parahippocampal gyrus (PHL/PHR). As showed in Figure 4, the generated waveforms demonstrate a high degree of fidelity to the ground truth signals, successfully capturing the principal morphological characteristics and temporal dynamics. The model effectively replicates both the slower, underlying oscillations and the sharper, transient features of the native iEEG. The alignment is particularly strong in regions such as the amygdala and the parahippocampal gyrus, where the generated signals closely trace the contours of the ground truth waveforms in terms of phase and relative amplitude.

In more structurally complex or deeper regions, such as the anterior hippocampus and entorhinal cortex, the model still captures the general trend of the signal but occasionally shows minor discrepancies in peak amplitude or precise temporal alignment. For instance, some of the fast transients in the ground truth signal are slightly smoothed or have a marginally lower amplitude in the generated counterpart. Nevertheless, the overall correspondence remains robust, underscoring NeuroFlowNet’s capability to learn the complex conditional mapping from non-invasive sEEG to invasive iEEG signals across multiple anatomical targets. This visual evidence corroborates that the model generates temporally coherent and physiologically plausible iEEG waveforms.

To quantify the temporal waveform performance metrics of the model (mean absolute error (MAE), Pearson correlation coefficient (Corr), and cosine similarity), Table 2 summarizes the results for multiple MTL subregions

Table 1: Subject Characteristics

No.	Age	Sex	Pathology	Implanted electrodes	Sessions
1	24	F	Xanthoastrocytoma WHO II	F3, F4, C3, C4, P3, P4, O1, O2, F7, F8, T3, T4, T5, T6, Fz, Cz, Pz, A1, A2 AHL, AL, ECL, LR, PHL, PHR	4
2	39	M	Gliosis	F3, F4, C3, C4, O1, O2, A1, A2 AHL, AHR, AL, AR, ECL, ECR, PHL, PHR	7
3	18	F	Hippocampal sclerosis	F3, F4, C3, C4, O1, O2, A1, A2 AHL, AHR, AL, ECL, PHL	3
4	28	M	Brain contusion	F3, F4, C3, C4, P3, P4, O1, O2, F7, F8, T3, T4, T5, T6, Fz, Cz, Pz, A1, A2 AHL, AHR, AL, AR, ECL, ECR, PHL, PHR	2
5	20	F	Focal cortical dysplasia	Fp1, Fp2, F3, F4, C3, C4, P3, P4, O1, O2, F7, F8, T4, T5, T6, Fz, Cz, Pz, A1, A2 AHL, AL, DRR, PHR	3
6	31	M	Hippocampal sclerosis	Fp1, Fp2, F3, F4, C3, C4, O1, O2, A1, A2 AHL, AHR, AL, AR, ECL, ECR, PHL, PHR	7
7	47	M	Hippocampal sclerosis	F3, F4, C3, C4, O1, O2, A1, A2 AHL, AHR, AL, AR, ECL, ECR, PHL, PHR	4
8	56	F	Hippocampal sclerosis	F3, F4, C3, C4, P3, P4, O1, O2, F7, F8, T3, T4, T5, T6, Fz, Cz, Pz, A1, A2 AHL, AHR, AL, AR, ECL, ECR, PHL, PHR	5
9	19	F	Hippocampal sclerosis	F3, F4, C3, C4, O1, O2, A1, A2 AHL, AHR, AL, AR, ECL, ECR, PHL, PHR	2

<sup>1</sup> Each iEEG electrode label corresponds to eight depth microelectrode contacts positioned along a single trajectory.

<sup>2</sup> Abbreviations for MTL Regions: AHL/AHR - Anterior Hippocampus (Left/Right), AL/AR - Amygdala (Left/Right), ECL/ECR - Entorhinal Cortex (Left/Right), PHL/PHR - Parahippocampal Gyrus (Left/Right), LR - Lateral Rhinal Area, DRR - Dorsal Rhinal Region.

across three subjects (S1, S6, S9). The results demonstrate that NeuroFlowNet exhibits varying efficacy in restoring the temporal dynamics of iEEG signals from different MTL subregions

Specifically, consistent with anatomical proximity to the scalp, more superficial or lateral regions such as the amygdala (AL/AR) and parahippocampal gyrus (PHL/PHR) generally show higher correlations and cosine similarities. For example, in subject S9, the parahippocampal gyrus (PHL) achieves a correlation coefficient of  $0.73 \pm 0.20$  and a cosine similarity of  $0.78 \pm 0.17$ , indicating strong alignment in waveform shape and direction. In contrast, deeper structures like the anterior hippocampus (AHL/AHR) present greater challenges: subject S1’s AHL region shows notably lower performance (Corr:  $0.35 \pm 0.28$ , Cosine:  $0.47 \pm 0.24$ ), reflecting difficulties in capturing the complex signal dynamics of deep brain areas.

Notably, MAE values often diverge from correlation metrics. For instance, in subject S6’s entorhinal cortex (ECL), a moderate correlation ( $0.49 \pm 0.23$ ) coexists with a relatively high MAE ( $53.71 \pm 21.22 \mu\text{V}$ ), suggesting potential discrepancies in amplitude scaling. Such inconsistencies may stem from the model’s sensitivity to inter-individual variations in signal amplitude and anatomical differences in electrode implantation locations.

#### 4.2. Power Spectral Density Comparison

To evaluate the frequency reproduction capability of NeuroFlowNet for iEEG signals, Figure 5 shows a comparison of the PSD waveforms of the generated signals (orange) and the actual signals (blue) for eight MTL subregions of subject S6. The PSD waveform for each region is the average of all electrodes in that region.

The analysis reveals that NeuroFlowNet successfully captures the salient spectral characteristics of the native iEEG signals. Across all depicted regions, the generated PSDs closely mirror the ground truth, particularly in replicating the prominent power peak in the alpha band (8-13 Hz) and a secondary peak in the theta band (4-8 Hz) [40, 41]. These frequency bands are physiologically critical in the MTL; theta oscillations are integral to memory encoding and retrieval, while alpha rhythms are associated with functional inhibition and attentional modulation. The model’s accurate generation of these peaks indicates that it learns to infer the state of these underlying cognitive processes from the conditioning sEEG data. Furthermore, the model correctly reproduces the aperiodic, 1/f-like decay in power at higher frequencies, a hallmark of background neural activity [42, 43]. This demonstrates a robust generalization beyond just the dominant oscillatory components.

To further scrutinize the model’s performance on the functionally significant alpha band, Figure 6 provides a detailed analysis of generated versus true alpha power. The scatter plot (Figure 6a) shows a strong positive correlation, with the linear fit line ( $y=0.67x+0.13$ ) closely following the ideal line ( $y=x$ ). This indicates that the model reliably

Table 2: Performance of NeuroFlowNet on iEEG signal generation.

Subject	Region	Temporal waveform			PSD waveform (0.5-50Hz)		Alpha PSD waveform (8-13Hz)		
		MAE ( $\mu$ V)	Corr	Cosine	Corr	Cosine	Corr	Cosine	Power MAPE (%)
S1	AHL	40.66 $\pm$ 21.53	0.35 $\pm$ 0.28	0.47 $\pm$ 0.24	0.66 $\pm$ 0.22	0.70 $\pm$ 0.19	0.25 $\pm$ 0.53	0.70 $\pm$ 0.21	2.65 $\pm$ 4.40
	AL	42.82 $\pm$ 28.98	0.39 $\pm$ 0.30	0.50 $\pm$ 0.26	0.67 $\pm$ 0.23	0.71 $\pm$ 0.20	0.29 $\pm$ 0.52	0.71 $\pm$ 0.21	3.33 $\pm$ 7.35
	ECL	49.15 $\pm$ 27.35	0.40 $\pm$ 0.25	0.50 $\pm$ 0.21	0.66 $\pm$ 0.24	0.70 $\pm$ 0.21	0.32 $\pm$ 0.52	0.72 $\pm$ 0.21	6.49 $\pm$ 16.65
	LR	33.86 $\pm$ 20.08	0.60 $\pm$ 0.28	0.65 $\pm$ 0.25	0.76 $\pm$ 0.23	0.79 $\pm$ 0.20	0.45 $\pm$ 0.48	0.78 $\pm$ 0.18	1.24 $\pm$ 2.18
	PHL	35.68 $\pm$ 15.08	0.56 $\pm$ 0.33	0.62 $\pm$ 0.28	0.74 $\pm$ 0.23	0.77 $\pm$ 0.20	0.44 $\pm$ 0.49	0.77 $\pm$ 0.20	1.23 $\pm$ 2.87
	PHR	82.42 $\pm$ 72.44	0.24 $\pm$ 0.29	0.39 $\pm$ 0.27	0.53 $\pm$ 0.25	0.59 $\pm$ 0.22	0.23 $\pm$ 0.53	0.70 $\pm$ 0.20	2.85 $\pm$ 5.36
S6	AHL	44.08 $\pm$ 27.47	0.44 $\pm$ 0.23	0.51 $\pm$ 0.21	0.61 $\pm$ 0.21	0.67 $\pm$ 0.18	0.33 $\pm$ 0.51	0.74 $\pm$ 0.19	1.58 $\pm$ 3.63
	AHR	40.80 $\pm$ 21.73	0.58 $\pm$ 0.21	0.63 $\pm$ 0.19	0.68 $\pm$ 0.20	0.73 $\pm$ 0.17	0.48 $\pm$ 0.50	0.80 $\pm$ 0.19	0.95 $\pm$ 1.88
	AL	45.78 $\pm$ 19.99	0.46 $\pm$ 0.23	0.52 $\pm$ 0.21	0.63 $\pm$ 0.21	0.67 $\pm$ 0.18	0.39 $\pm$ 0.48	0.76 $\pm$ 0.19	1.75 $\pm$ 2.97
	AR	26.77 $\pm$ 9.21	0.74 $\pm$ 0.16	0.77 $\pm$ 0.14	0.78 $\pm$ 0.17	0.81 $\pm$ 0.15	0.67 $\pm$ 0.38	0.87 $\pm$ 0.14	0.61 $\pm$ 1.01
	ECL	53.71 $\pm$ 21.22	0.49 $\pm$ 0.23	0.54 $\pm$ 0.21	0.67 $\pm$ 0.21	0.71 $\pm$ 0.18	0.37 $\pm$ 0.51	0.75 $\pm$ 0.19	1.75 $\pm$ 3.41
	ECR	34.92 $\pm$ 14.32	0.64 $\pm$ 0.17	0.68 $\pm$ 0.16	0.71 $\pm$ 0.20	0.75 $\pm$ 0.18	0.59 $\pm$ 0.43	0.84 $\pm$ 0.15	1.05 $\pm$ 2.48
	PHL	25.73 $\pm$ 15.79	0.39 $\pm$ 0.29	0.49 $\pm$ 0.25	0.60 $\pm$ 0.21	0.66 $\pm$ 0.18	0.32 $\pm$ 0.51	0.74 $\pm$ 0.20	1.38 $\pm$ 2.51
	PHR	36.89 $\pm$ 16.07	0.60 $\pm$ 0.20	0.64 $\pm$ 0.18	0.70 $\pm$ 0.19	0.74 $\pm$ 0.17	0.51 $\pm$ 0.45	0.79 $\pm$ 0.18	0.84 $\pm$ 1.53
S9	AHL	29.92 $\pm$ 10.79	0.67 $\pm$ 0.19	0.73 $\pm$ 0.15	0.81 $\pm$ 0.17	0.82 $\pm$ 0.16	0.36 $\pm$ 0.49	0.73 $\pm$ 0.20	0.88 $\pm$ 1.24
	AHR	43.49 $\pm$ 26.44	0.38 $\pm$ 0.28	0.50 $\pm$ 0.24	0.69 $\pm$ 0.23	0.71 $\pm$ 0.21	0.20 $\pm$ 0.55	0.67 $\pm$ 0.22	7.20 $\pm$ 14.62
	AL	35.30 $\pm$ 11.46	0.61 $\pm$ 0.19	0.66 $\pm$ 0.16	0.78 $\pm$ 0.19	0.80 $\pm$ 0.17	0.34 $\pm$ 0.50	0.72 $\pm$ 0.21	1.45 $\pm$ 3.01
	AR	29.48 $\pm$ 21.12	0.34 $\pm$ 0.34	0.46 $\pm$ 0.30	0.64 $\pm$ 0.25	0.68 $\pm$ 0.22	0.22 $\pm$ 0.54	0.67 $\pm$ 0.23	4.82 $\pm$ 8.81
	ECL	38.73 $\pm$ 17.66	0.55 $\pm$ 0.25	0.61 $\pm$ 0.21	0.75 $\pm$ 0.22	0.77 $\pm$ 0.20	0.34 $\pm$ 0.52	0.72 $\pm$ 0.22	1.62 $\pm$ 2.73
	ECR	43.11 $\pm$ 18.69	0.44 $\pm$ 0.26	0.51 $\pm$ 0.23	0.71 $\pm$ 0.22	0.74 $\pm$ 0.20	0.24 $\pm$ 0.52	0.70 $\pm$ 0.21	3.46 $\pm$ 5.78
	PHL	26.60 $\pm$ 14.10	0.73 $\pm$ 0.20	0.78 $\pm$ 0.17	0.84 $\pm$ 0.16	0.85 $\pm$ 0.15	0.46 $\pm$ 0.46	0.77 $\pm$ 0.18	0.93 $\pm$ 1.39
	PHR	38.48 $\pm$ 17.46	0.49 $\pm$ 0.26	0.55 $\pm$ 0.25	0.74 $\pm$ 0.22	0.76 $\pm$ 0.20	0.33 $\pm$ 0.51	0.71 $\pm$ 0.21	5.35 $\pm$ 10.49

<sup>1</sup> The results of each region are averaged across all electrodes within that region.

<sup>2</sup> Abbreviations for MTL Regions: AHL/AHR - Anterior Hippocampus (Left/Right), AL/AR - Amygdala (Left/Right), ECL/ECR - Entorhinal Cortex (Left/Right), PHL/PHR - Parahippocampal Gyrus (Left/Right), LR - Lateral Rhinal Area.

captures the relative changes in alpha power. The slope of less than one suggests a slight regression to the mean, where the model may temper the most extreme high or low power values, a common characteristic when inferring high-resolution signals from lower signal-to-noise data.

The Bland-Altman plot (Figure 6b) reinforces this finding by showing that the mean difference between true and generated alpha power is exceptionally low (0.01), indicating no systematic bias in the model’s predictions. The data points are evenly scattered within the 95% limits of agreement, confirming that while individual predictions have some variance, the model’s estimations are, on average, highly accurate. Collectively, the spectral analysis demonstrates that NeuroFlowNet generates iEEG signals that are not only temporally plausible but also spectrally realistic, preserving the key neurophysiological frequency fingerprints essential for downstream analysis.

To quantify the frequency domain reproduction capability of the model, Table 2 summarizes the results for multiple MTL subregions of three subjects (S1, S6, and S9), 0.5-50 Hz PSD waveform metrics (Corr and cosine similarity), and 8-13 Hz  $\alpha$  PSD waveform metrics (Corr, cosine similarity, and mean absolute percentage error (MAPE)).

In the broad frequency range (0.5-50 Hz), NeuroFlowNet demonstrates relatively stable performance across MTL regions. PSD correlation coefficients range from  $0.53 \pm 0.25$  (PHR, S1) to  $0.84 \pm 0.16$  (PHL, S9), indicating reliable preservation of spectral composition despite temporal waveform variability. While most regions exhibit PSD cosine similarities exceeding 0.70, an exception is observed in S1’s PHR region ( $0.59 \pm 0.22$ ), highlighting minor regional variability.

For the alpha band (8-13 Hz), cosine similarities remain stable (0.70-0.87), but correlations fluctuate significantly, such as  $0.22 \pm 0.54$  in S9’s AR region versus  $0.67 \pm 0.38$  in S6’s AR region. Alpha power MAPE is generally low (below 3% for most regions), but outliers include S1’s ECL (6.49  $\pm$  16.65%), S9’s AHR (7.20  $\pm$  14.62%), and S9’s PHR (5.35  $\pm$  10.49%). This suggests the model struggles with precise alpha-phase capture but effectively estimates relative power distributions, critical for neurophysiological applications focusing on oscillatory activity [44, 45, 46].

### 4.3. Inter-Channel Correlation Comparison

Beyond generating realistic single-channel waveforms, a crucial test for the model is its ability to capture the complex functional relationships between different neural populations. These relationships are reflected in the inter-

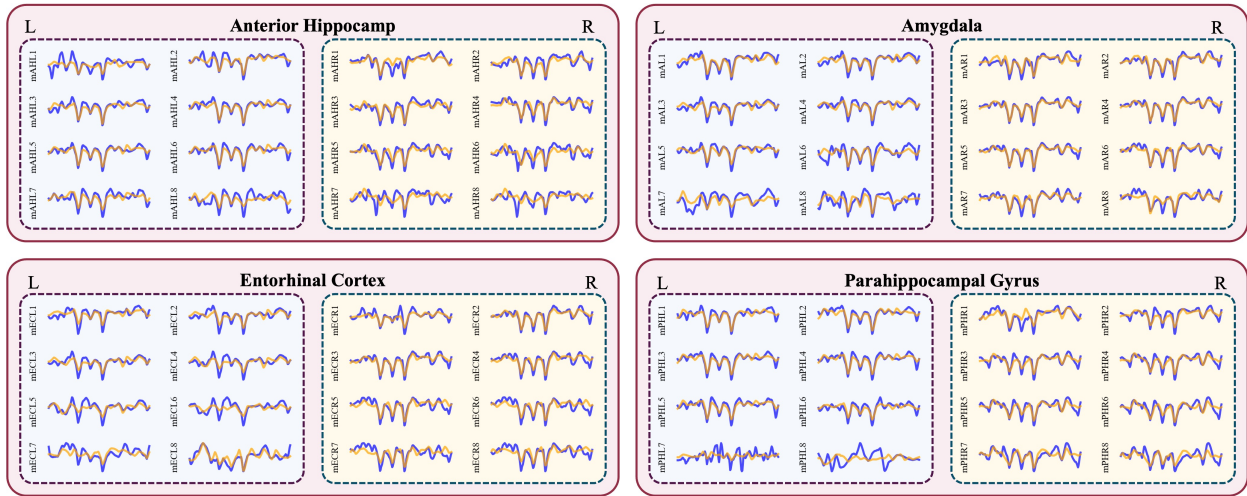


Figure 4: Exemplar generated iEEG signals (orange) overlaid with ground truth iEEG signals (blue) for various MTL subregions, specifically showing a 200ms segment from Subject S6. The figure illustrates the performance of NeuroFlowNet in generating iEEG signals from sEEG data across different anatomical targets, including anterior hippocampus (AHL/AHR), amygdala (AL/AR), entorhinal cortex (ECL/ECR), and parahippocampal gyrus (PHL/PHR).

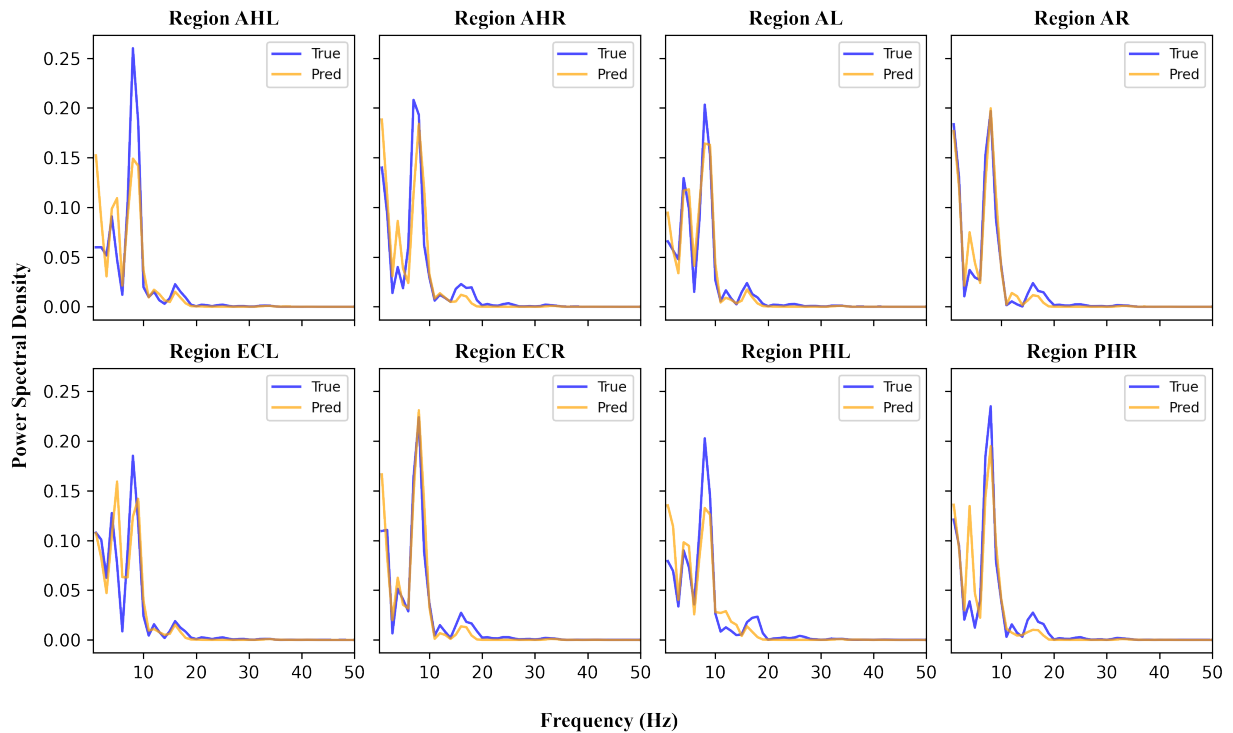
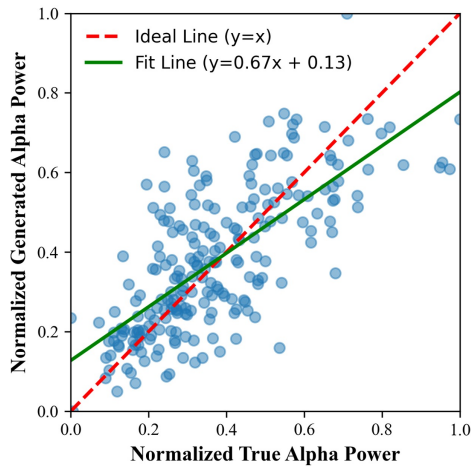
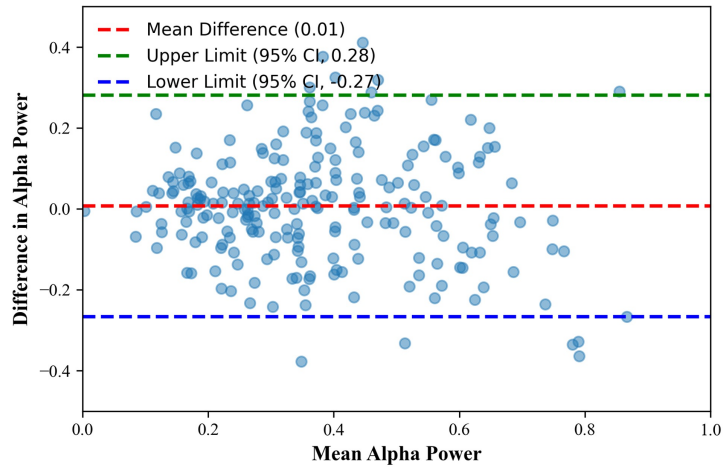


Figure 5: Comparison of power spectral density (PSD) between ground truth iEEG signals (blue) and generated iEEG signals (orange) for a 200 ms segment from Subject S6. The figure shows the average PSD across all electrodes within each MTL subregion, including anterior hippocampus (AHL/AHR), amygdala (AL/AR), entorhinal cortex (ECL/ECR), and parahippocampal gyrus (PHL/PHR).

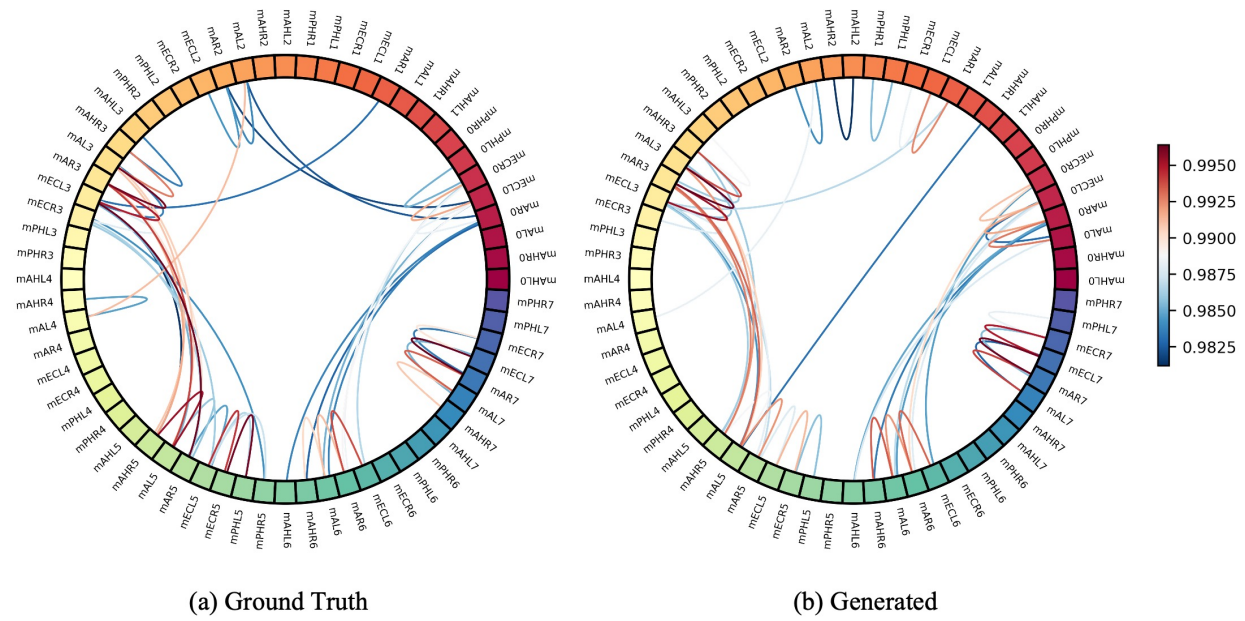


(a) Alpha Power Scatter Plot



(b) Bland-Altman Plot for Alpha Power

Figure 6: (a) Scatter plot of normalized true alpha power versus normalized generated alpha power. The red dashed line represents the ideal line ( $y = x$ ), while the green solid line indicates the linear fit ( $y = 0.67x + 0.13$ ). (b) Bland-Altman plot showing the difference in alpha power against the mean alpha power. The red dashed line indicates the mean difference (0.01), and the green and blue dashed lines represent the upper (95% CI, 0.28) and lower (95% CI, -0.27) limits of agreement, respectively.



(a) Ground Truth

(b) Generated

Figure 7: Comparison of inter-channel correlation. Circular graphs show the connectivity patterns of (a) the original iEEG signals and (b) the generated iEEG signals. Both plots illustrate a 200 ms segment from Subject S6. Pairwise Pearson correlation coefficients are computed between all channels, and only the top 50 strongest absolute correlations are visualized for clarity.

channel correlation structure of the iEEG signals. Figure 7 presents a qualitative comparison of these correlation patterns, displaying the 50 strongest pairwise Pearson correlations for both the ground truth (a) and generated (b) iEEG signals from a 200ms segment of Subject S6.

The circular plots reveal a remarkable correspondence between the ground truth and the generated data. The model successfully reproduces the salient features of the functional connectivity network. Key patterns, such as strong correlations between homologous regions in the left and right hemispheres (e.g., between channels in AHL and AHR), are clearly preserved. This is physiologically significant as it reflects the synchronous activity maintained between bilateral structures via commissural pathways.

Furthermore, the model accurately captures strong correlations between anatomically and functionally connected regions within the same hemisphere, such as the connections between the entorhinal cortex and the hippocampus, which form a critical circuit for memory processing. The visual similarity of the two plots—from the dense connections within the parahippocampal gyrus to the sparser but strong links spanning distant regions—indicates that NeuroFlowNet is not merely generating a collection of independent, albeit realistic, time series. Instead, it is learning the underlying covariance structure that governs the system-level dynamics of the Medial Temporal Lobe network. This ability to replicate the spatial organization of neural activity is a strong indicator that the generated iEEG data retains the neurophysiological signatures necessary for more advanced network-level analyses.

#### 4.4. Discussion of Physiological Determinants in Regional Variability

The observed performance heterogeneity across MTL subregions can be partially attributed to neuroanatomical and physiological factors. In terms of structural complexity, the anterior hippocampus (AHL/AHR) is characterized by intricate laminar organization and high neuronal density, resulting in complex and non-linear iEEG signal patterns [47]. This complexity likely exceeds the current representational capacity of NeuroFlowNet’s conditional normalizing flow, contributing to reduced fidelity in this region [48]. Besides, deeply situated structures like AHL experience greater signal attenuation in sEEG recordings due to intervening tissues (cerebrospinal fluid, skull), reducing the signal-to-noise ratio of the conditioning data and complicating accurate inference of iEEG dynamics [49]. In contrast, more superficial regions such as the parahippocampal gyrus benefit from proximity to the cortical surface, aiding model performance [50]. Additionally, regions with strong cortico-MTL connectivity, such as the entorhinal cortex (ECL/ECR), may exhibit iEEG dynamics that are more inferable from scalp-recorded potentials, aligning with their relatively high temporal and spectral performance [51].

## 5. Conclusion

In this study, we introduced NeuroFlowNet, a novel generative framework based on conditional normalizing flows, to address the enduring challenge of generating high-fidelity iEEG from non-invasive sEEG. Our work makes a pivotal contribution by demonstrating, for the first time, the feasibility of reconstructing iEEG signals across the entire deep temporal lobe. By directly modeling the conditional probability distribution, NeuroFlowNet fundamentally overcomes the mode collapse and deterministic mapping limitations of previous generative models. Our results confirm that the generated signals not only achieve high fidelity in temporal waveforms and spectral characteristics but also successfully preserve the complex inter-channel correlation structure, reflecting the underlying functional connectivity of the MTL network. The ability to generate realistic, probabilistic iEEG provides a powerful new tool for both clinical and research applications, offering a non-invasive window into deep brain dynamics. This could significantly improve our understanding of cognitive processes governed by the MTL, potentially reducing the reliance on high-risk invasive procedures.

However, we acknowledge certain limitations. The model’s performance exhibits variability across different MTL subregions, with deeper and more structurally complex areas like the anterior hippocampus proving more challenging to reconstruct accurately. This suggests that the signal-to-noise ratio of the conditioning sEEG and the inherent complexity of the target signal are key performance determinants. Future work will focus on three main directions: 1) Enhancing the model architecture by incorporating more sophisticated conditioning mechanisms that can better leverage spatial information from the sEEG montage. 2) Expanding the framework to a subject-independent model by developing advanced domain adaptation techniques to account for inter-subject anatomical and physiological variability. 3) Validating the clinical utility of the generated iEEG in downstream tasks, such as automated seizure detection and cognitive state decoding, to bridge the gap between technical innovation and practical application.

## **CRedit authorship contribution statement**

**Dongyi He:** Conceptualization, Methodology, Software, Data curation, Writing - original draft, Writing - review & editing, Visualization. **Bin Jiang:** Conceptualization, Supervision, Writing - review & editing, Funding acquisition, Writing - original draft, Formal analysis. **Kecheng Feng:** Writing - review & editing, Visualization, Formal analysis. **Luyin Zhang:** Writing - review & editing. **Ling Liu:** Writing - review & editing. **Yuxuan Li:** Writing - review & editing. **Yun Zhao:** Funding acquisition, Formal analysis, Writing - review & editing, Supervision, Resources **He Yan:** Supervision, Resources **All authors have read and approved the final manuscript.**

## **Declaration of competing interest**

The authors declare that they have no known competing financial interests or personal relationships that could have appeared to influence the work reported in this paper.

## **Ethics statement**

This study was conducted in publicly available datasets, thus ethical approval was not required.

## **Declaration of generative AI and AI-assisted technologies in the writing process.**

During the preparation of this work the author(s) used ChatGPT in order to check the grammar and spelling of the manuscript. After using this tool/service, the author(s) reviewed and edited the content as needed and take(s) full responsibility for the content of the published article.

## **Funding Declaration**

This research was funded by the Scientific and Technological Research Program of the Chongqing Education Commission (KJZD-K202303103, KJQN202501104) and Chongqing Municipal Key Project for Technology Innovation and Application Development (CSTB2024TIAD-KPX0042).

## **References**

- [1] A. Craik, Y. He, J. L. Contreras-Vidal, Deep learning for electroencephalogram (eeg) classification tasks: a review, *Journal of neural engineering* 16 (3) (2019) 031001.
- [2] A. Kumari, D. R. Edla, A study on brain-computer interface: Methods and applications, *SN Computer Science* 4 (2) (2022) 98.
- [3] C. M. Michel, D. Brunet, Eeg source imaging: a practical review of the analysis steps, *Frontiers in neurology* 10 (2019) 325.
- [4] A. Biasiucci, R. Leeb, I. Iturrate, S. Perdakis, A. Al-Khodairy, T. Corbet, A. Schnider, T. Schmidlin, H. Zhang, M. Bassolino, et al., Brain-actuated functional electrical stimulation elicits lasting arm motor recovery after stroke, *Nature communications* 9 (1) (2018) 2421.
- [5] M. Hassan, F. Wendling, Electroencephalography source connectivity: aiming for high resolution of brain networks in time and space, *IEEE Signal Processing Magazine* 35 (3) (2018) 81–96.
- [6] B. He, L. Astolfi, P. A. Valdés-Sosa, D. Marinazzo, S. O. Palva, C.-G. Bénar, C. M. Michel, T. Koenig, Electrophysiological brain connectivity: theory and implementation, *IEEE transactions on biomedical engineering* 66 (7) (2019) 2115–2137.

- [7] X. Ma, W. Chen, Z. Pei, Y. Zhang, J. Chen, Attention-based convolutional neural network with multi-modal temporal information fusion for motor imagery eeg decoding, *Computers in Biology and Medicine* 175 (2024) 108504.
- [8] N. Padfield, J. Zabalza, H. Zhao, V. Masero, J. Ren, Eeg-based brain-computer interfaces using motor-imagery: Techniques and challenges, *Sensors* 19 (6) (2019) 1423.
- [9] J. Parvizi, S. Kastner, Human intracranial eeg: promises and limitations, *Nature neuroscience* 21 (4) (2018) 474.
- [10] J. Parvizi, S. Kastner, Promises and limitations of human intracranial electroencephalography, *Nature neuroscience* 21 (4) (2018) 474–483.
- [11] R. Mukamel, I. Fried, Human intracranial recordings and cognitive neuroscience, *Annual review of psychology* 63 (1) (2012) 511–537.
- [12] R. Grech, T. Cassar, J. Muscat, K. P. Camilleri, S. G. Fabri, M. Zervakis, P. Xanthopoulos, V. Sakkalis, B. Vanrumste, Review on solving the inverse problem in eeg source analysis, *Journal of neuroengineering and rehabilitation* 5 (1) (2008) 25.
- [13] S. M. M. Basri, H. Al-Nashash, H. Mir, Inverse problem for m/eeg source localization: a review, *IEEE Sensors Journal* (2024).
- [14] S. Baillet, Magnetoencephalography for brain electrophysiology and imaging, *Nature neuroscience* 20 (3) (2017) 327–339.
- [15] A. Sohrabpour, Y. Lu, P. Kankirawatana, J. Blount, H. Kim, B. He, Effect of eeg electrode number on epileptic source localization in pediatric patients, *Clinical Neurophysiology* 126 (3) (2015) 472–480.
- [16] T. Hedrich, G. Pellegrino, E. Kobayashi, J.-M. Lina, C. Grova, Comparison of the spatial resolution of source imaging techniques in high-density eeg and meg, *Neuroimage* 157 (2017) 531–544.
- [17] B. He, A. Sohrabpour, E. Brown, Z. Liu, Electrophysiological source imaging: a noninvasive window to brain dynamics, *Annual review of biomedical engineering* 20 (1) (2018) 171–196.
- [18] M. Seeber, L.-M. Cantonas, M. Hoevels, T. Sesia, V. Visser-Vandewalle, C. M. Michel, Subcortical electrophysiological activity is detectable with high-density eeg source imaging, *Nature communications* 10 (1) (2019) 753.
- [19] P. Ryvlin, Seeg in 2025: progress and pending challenges in stereotaxy methods, biomarkers and radiofrequency thermocoagulation, *Current opinion in neurology* 38 (2) (2025) 111–120.
- [20] C. Herff, D. J. Krusienski, P. Kubben, The potential of stereotactic-eeg for brain-computer interfaces: current progress and future directions, *Frontiers in neuroscience* 14 (2020) 123.
- [21] S. K. Veeramalla, V. H. R. Talari, Multiple dipole source localization of eeg measurements using particle filter with partial stratified resampling, *Biomedical engineering letters* 10 (2) (2020) 205–215.
- [22] T. R. Knösche, M. Gräser, A. Anwander, Prior knowledge on cortex organization in the reconstruction of source current densities from eeg, *Neuroimage* 67 (2013) 7–24.
- [23] R. R. Ramírez, D. Wipf, S. Baillet, Neuroelectromagnetic source imaging of brain dynamics, in: *Computational Neuroscience*, Springer, 2010, pp. 127–155.
- [24] S. Cui, L. Duan, B. Gong, Y. Qiao, F. Xu, J. Chen, C. Wang, Eeg source localization using spatio-temporal neural network, *China Communications* 16 (7) (2019) 131–143.
- [25] M. Saeidi, W. Karwowski, F. V. Farahani, K. Fiok, R. Taiar, P. A. Hancock, A. Al-Juaid, Neural decoding of eeg signals with machine learning: a systematic review, *Brain sciences* 11 (11) (2021) 1525.

- [26] F. Hassan, S. F. Hussain, Review of eeg signals classification using machine learning and deep-learning techniques, in: *Advances in non-invasive biomedical signal sensing and processing with machine learning*, Springer, 2023, pp. 159–183.
- [27] J. Rong, R. Sun, B. Joseph, G. Worrell, B. He, Deep learning-based eeg source imaging is robust under varying electrode configurations, *Clinical Neurophysiology* (2025).
- [28] L. Bozhkov, P. Georgieva, Overview of deep learning architectures for eeg-based brain imaging, in: *2018 International joint conference on neural networks (IJCNN)*, IEEE, 2018, pp. 1–7.
- [29] Z. Hui, L. Ying, W. Lingyue, Y. Ning, Y. Shuo, Eeg dipole source localization using deep neural network, *Int. J. Circuits Syst. Signal Process* 16 (2022) 132–140.
- [30] L. Hecker, R. Rupprecht, L. Tebartz Van Elst, J. Kornmeier, Convdip: A convolutional neural network for better eeg source imaging, *Frontiers in Neuroscience* 15 (2021) 569918.
- [31] G. Huang, K. Liu, J. Liang, C. Cai, Z. H. Gu, F. Qi, Y. Li, Z. L. Yu, W. Wu, Electromagnetic source imaging via a data-synthesis-based convolutional encoder–decoder network, *IEEE Transactions on Neural Networks and Learning Systems* 35 (5) (2022) 6423–6437.
- [32] S. M. Kaviri, R. Vinjamuri, Integrating electroencephalography source localization and residual convolutional neural network for advanced stroke rehabilitation, *Bioengineering* 11 (10) (2024) 967.
- [33] J. C. Bore, P. Li, L. Jiang, W. M. Ayedh, C. Chen, D. J. Harmah, D. Yao, Z. Cao, P. Xu, A long short-term memory network for sparse spatiotemporal eeg source imaging, *IEEE Transactions on Medical Imaging* 40 (12) (2021) 3787–3800.
- [34] A. Sikka, H. Jamalabadi, M. Krylova, S. Alizadeh, J. N. Van Der Meer, L. Danyeli, M. Deliano, P. Vicheva, T. Hahn, T. Koenig, et al., Investigating the temporal dynamics of electroencephalogram (eeg) microstates using recurrent neural networks, *Human brain mapping* 41 (9) (2020) 2334–2346.
- [35] M. Doan, S. Plis, Scaling synthetic brain data generation, *IEEE Journal of Biomedical and Health Informatics* (2024).
- [36] G. Cisotto, A. Zancanaro, I. F. Zoppis, S. L. Manzoni, hveegnet: a novel deep learning model for high-fidelity eeg reconstruction, *Frontiers in Neuroinformatics* 18 (2024) 1459970.
- [37] B. Abdi-Sargezeh, A. Oswal, S. Sanei, Mapping scalp to intracranial eeg using generative adversarial networks for automatically detecting interictal epileptiform discharges, in: *2023 IEEE Statistical Signal Processing Workshop (SSP)*, IEEE, 2023, pp. 710–714.
- [38] B. Abdi-Sargezeh, S. Shirani, A. Valentin, G. Alarcon, S. Sanei, Eeg-to-eeg: Scalp-to-intracranial eeg translation using a combination of variational autoencoder and generative adversarial networks, *Sensors* 25 (2) (2025) 494.
- [39] E. Boran, T. Fedele, P. Klaver, P. Hilfiker, L. Stieglitz, T. Grunwald, J. Sarnthein, Persistent hippocampal neural firing and hippocampal-cortical coupling predict verbal working memory load, *Science advances* 5 (3) (2019) eaav3687.
- [40] N. A. Herweg, E. A. Solomon, M. J. Kahana, Theta oscillations in human memory, *Trends in cognitive sciences* 24 (3) (2020) 208–227.
- [41] O. Jensen, A. Mazaheri, Shaping functional architecture by oscillatory alpha activity: gating by inhibition, *Frontiers in human neuroscience* 4 (2010) 186.
- [42] B. J. He, Scale-free brain activity: past, present, and future, *Trends in cognitive sciences* 18 (9) (2014) 480–487.
- [43] M. A. Kramer, C. J. Chu, The 1/f-like behavior of neural field spectra are a natural consequence of noise driven brain dynamics, *bioRxiv* (2023).

- [44] G. Assenza, F. Capone, L. Di Biase, F. Ferreri, L. Florio, A. Guerra, M. Marano, M. Paolucci, F. Ranieri, G. Salomone, et al., Oscillatory activities in neurological disorders of elderly: biomarkers to target for neuro-modulation, *Frontiers in Aging Neuroscience* 9 (2017) 189.
- [45] P. J. Uhlhaas, W. Singer, Neural synchrony in brain disorders: relevance for cognitive dysfunctions and patho-physiology, *neuron* 52 (1) (2006) 155–168.
- [46] Q. Zhou, J. Lin, L. Yao, Y. Wang, Y. Han, K. Xu, Relative power correlates with the decoding performance of motor imagery both across time and subjects, *Frontiers in Human Neuroscience* 15 (2021) 701091.
- [47] G. Li, S. Jiang, S. E. Paraskevopoulou, M. Wang, Y. Xu, Z. Wu, L. Chen, D. Zhang, G. Schalk, Optimal referencing for stereo-electroencephalographic (seeg) recordings, *NeuroImage* 183 (2018) 327–335.
- [48] C. Winkler, D. Worrall, E. Hoogeboom, M. Welling, Learning likelihoods with conditional normalizing flows, *arXiv preprint arXiv:1912.00042* (2019).
- [49] M. F. Hnazaee, B. Wittevrongel, E. Khachatryan, A. Libert, E. Carrette, I. Dauwe, A. Meurs, P. Boon, D. Van Roost, M. M. Van Hulle, Localization of deep brain activity with scalp and subdural eeg, *NeuroImage* 223 (2020) 117344.
- [50] K. Vlcek, I. Fajnerova, T. Nekovarova, L. Hejtmanek, R. Janca, P. Jezdik, A. Kalina, M. Tomasek, P. Krsek, J. Hammer, et al., Mapping the scene and object processing networks by intracranial eeg, *Frontiers in human neuroscience* 14 (2020) 561399.
- [51] J. Yang, D. Cao, C. Guo, L. Stieglitz, D. Ledergerber, J. Sarnthein, J. Li, Enhanced role of the entorhinal cortex in adapting to increased working memory load, *Nature Communications* 16 (1) (2025) 5798.